

# Exact Ground-State Properties of Strongly Interacting Fermi Gases in Two Dimensions

Hao Shi, Simone Chiesa, and Shiwei Zhang

*Department of Physics, The College of William and Mary, Williamsburg, Virginia 23187*

Exact calculations are performed on the two-dimensional strongly interacting, unpolarized, uniform Fermi gas with a zero-range attractive interaction. Two auxiliary-field approaches are employed which accelerate the sampling of imaginary-time paths using BCS trial wave functions and a force bias technique. Their combination enables calculations on large enough lattices to reliably compute ground-state properties in the thermodynamic limit. A new equation of state is obtained, with a parametrization provided, which can serve as a benchmark and allow accurate comparisons with experiments. The pressure, contact parameter, and condensate fraction are determined systematically vs.  $k_F a$ . The momentum distribution, pairing correlation, and the structure of the pair wave function are computed. The use of force bias to accelerate the Metropolis sampling of auxiliary-fields in determinantal approaches is discussed.

PACS numbers: 03.75.Ss, 05.30.Fk, 02.70.Ss, 03.75.Hh

Exact results on fundamental models are uncommon, especially for strongly interacting fermion systems. In the rare cases where they exist (for example in one-dimensional models by Bethe ansatz or density matrix renormalization group [1, 2]), they have invariably played an integral role in bringing about physical insights, advancing our understanding, and serving as benchmarks for the development of new theoretical and computational approaches.

The Fermi gas with a zero-range attractive interactions is a model for strongly interacting fermions which has generated a great deal of research activities [3, 4]. The model is of interest in both condensed matter and nuclear physics. As a model it is rather unique in that, thanks to advances in experimental techniques using ultracold atoms, it can be realized in a laboratory with great precision and control [4, 5].

In three-dimensions (3D) the interplay between experiment, theory and computation has lead to rapid advances [6–9]. An example is seen in the evolution [10] of the determination of the so-called Bertsch parameter at unitarity. Quantitative comparisons have allowed validation of our understanding and provided an impetus for developments of both experimental and theoretical techniques. The remarkable level of agreement achieved recently between calculation [8] and experiment [7] demonstrates the tremendous progress towards precise understanding and control of strongly correlated quantum matter.

The two-dimensional (2D) Fermi gas has attracted considerable recent interest [11–19], especially with its experimental realization using highly anisotropic trapping potentials [20]. In 2D a bound state always exists, and the BCS-BEC cross-over offers rich possibilities between the interplay of inter-particle spacing (density) and interaction strength, where effects beyond the mean-field description will be more pronounced than in 3D. Interest in this model is further enhanced by the 2D nature of many of the most interesting and complex materials, including high- $T_c$  cuprate superconductors and topological superconductors [21].

In this paper, we obtain *exact* numerical results on the ground state of the strongly interacting 2D spin-balanced uniform Fermi gas. To date the most accurate numerical results on the 2D system have mainly come from diffusion Monte Carlo (DMC) simulations [18]. These calculations, however, involve the fixed-node approximation [22, 23] and lead to systematic errors which are difficult to estimate; furthermore, some of the correlation functions that are central to the physics of these systems are not readily available from DMC. Here, we employ two auxiliary-field quantum Monte Carlo (AFQMC) approaches: one based on the branching random walk method used in the 3D study in Ref. [8], and the other a novel approach in the Metropolis path-integral framework which dramatically improves efficiency. Their combination allows us to calculate the thermodynamics and pairing properties exactly in the entire range of interaction strengths.

Our calculations are performed on periodic lattices. We use supercells of up to 3,000 sites, containing about 120 particles, with projection length in imaginary time of  $\beta > 50$  (in units of  $1/E_F$ ). For each lattice and Hamiltonian parameters, the calculation is numerically exact, with only statistical uncertainties which are fully controlled. Systematic extrapolations are then carried out to reach the thermodynamic limit (TL).

As the interaction in cold atoms is short-ranged compared to the inter-particle spacing, the uniform 2D Fermi gas can be modeled by a lattice Hamiltonian

$$\hat{H} = t \sum_{\mathbf{k}, \sigma} \varepsilon_{\mathbf{k}} c_{\mathbf{k}\sigma}^\dagger c_{\mathbf{k}\sigma} + U \sum_i^{N_s} n_{i\uparrow} n_{i\downarrow} \quad (1)$$

with  $N_s = L^2$  sites and  $t = \hbar^2/(2m\Delta^2)$ , where  $\Delta$  is the lattice parameter. Only the low energy behavior of  $\varepsilon_{\mathbf{k}}$  will be relevant, and we have used both the Hubbard dispersion  $\varepsilon_{\mathbf{k}}^H = 4 - 2(\cos k_x + \cos k_y)$  and the quadratic dispersion  $\varepsilon_{\mathbf{k}}^q = k_x^2 + k_y^2$ . In this form, the momentum  $k_x$  (or  $k_y$ ) is defined on the lattice, with units  $2\pi/L$ , and  $k_x \in [-\pi, \pi)$ . The on-site interaction is attractive and is

given by [24]

$$\frac{U}{t} = -\frac{4\pi}{\ln(k_F a) - \ln(C\sqrt{n})}, \quad (2)$$

which is tuned, for each lattice density  $n \equiv N/\mathcal{N}_s$  and Fermi momentum  $k_F = \sqrt{2\pi n}/\Delta$ , to produce the desired 2D scattering length  $a$ , defined as the position of the node of the zero-energy  $s$ -wave solution of the two-body problem. The constant  $C$  in Eq. (2) depends on the dispersion relation:  $C^H = 0.49758$  and  $C^q = 0.80261$ .

We employ two AFQMC methods to study this model: the branching random walk approach, and an accelerated Metropolis approach with a force bias. In the first [8], we project the ground-state wave function by importance-sampled random walks in Slater determinant space [25, 26]. A BCS wave function, taken from the solution of the gap equation for the same discretized Hamiltonian, is chosen as the trial wave function, and the mixed estimator [8, 27] is used to calculate the ground-state energy. The BCS trial wave function shortens the convergence time in the imaginary-time projection, and greatly reduces the Monte Carlo statistical fluctuations, as illustrated in the 3D case [8].

Our second approach is based on the ground-state path integral form of AFQMC, but introduces several advances, including accelerated sampling (described in more detail in Appendix A) by a dynamic force bias [27], which enables global moves of fields on a time slice with acceptance ratio of over 90%, and control of the Monte Carlo variance [47]. Its main advantage over the the open-ended branching random walk approach is the ease with which any observables can be computed, and we use it to compute the momentum distribution and correlation functions. (Since there is no sign problem here, no constraint is needed, which is the primary motivation for using the open-ended branching random walk form.) With this approach, our calculations typically have  $\beta \sim 320$  or larger (in units of  $t^{-1}$ ), discretized with over 12,800 time-slices.

These technical advances result in orders of magnitude improvement in sampling efficiency, which makes it possible to achieve the high numerical accuracy presented in this work. In both approaches, the computational cost scales as  $\sim \mathcal{N}_s N^2 \beta$ . The linear scaling with  $\mathcal{N}_s$  is important, as it enables calculations on large lattice sizes. To approach the TL, we first extrapolate calculations to the continuum limit by taking  $\mathcal{N}_s \rightarrow \infty$  while holding  $N$  fixed. The number of particles,  $N$ , is then increased until convergence is reached within our statistical accuracy, as illustrated next.

Figure 1 displays the calculated equation of state (EOS), in units of the Fermi gas energy  $E_{FG} = \pi n t$ , as a function of the interacting strength,  $x \equiv \ln(k_F a)$ . A table of the AFQMC data can be found in Appendix C. The top panel illustrates the convergence to the TL, where AFQMC energies are shown for fixed  $N$ . At each  $x$ , the energy has been extrapolated to the continuum limit, using a 4th-order polynomial in  $1/L$ . In the more strongly

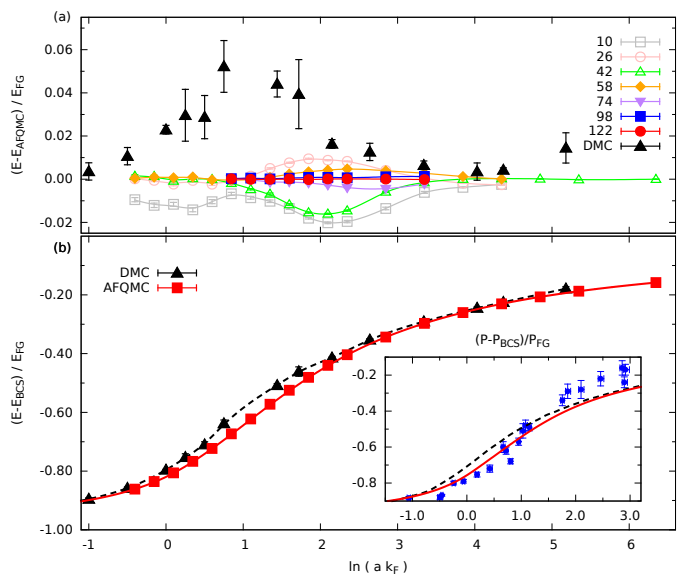


FIG. 1: (Color online) Calculated equation of state. The top panel shows the energy, relative to the final AFQMC results, for finite number of particles,  $N$ . Also shown are the DMC results of Ref. [18], which are variational. Note the small scale of the vertical axis. The bottom panel shows the AFQMC (and DMC) results at the TL, relative to the BCS result. A fit has been performed on the AFQMC results for the EOS. The result is given in Eqs. (4-5) and shown as the solid line. The inset in panel (b) compares the calculated pressure from AFQMC (solid line) and DMC (dashed, taken from Ref. [28]) with experiment [28] (points) in the crossover region.

interacting cases, we take advantage of the fact that  $\varepsilon_{\mathbf{k}}^q$  and  $\varepsilon_{\mathbf{k}}^H$  produce energies which converge to a common limit from opposite directions and perform both sets of calculations to reduce the uncertainty in the extrapolation. In the opposite regime, energies from the quadratic dispersion shows less dependence on  $L$  and they are used alone. We illustrate the extrapolation procedure in Appendix B. The error bar of each symbol, barely noticeable in the graph, combines the QMC statistical error (negligible) at each  $L$  and a conservative estimate of the uncertainty from the extrapolation, which typically involves half a dozen or more data points from each dispersion relation, with  $L$  ranging from  $\sim 15$  to 45 (and larger if necessary).

The results for different values of  $N$  show that convergence is reached to within our statistical accuracy by  $N \sim 100$  [29]. This is consistent with DMC results [18] which observed no significant change between  $N$  of 26 and 98. The DMC results provide the current best estimate of the EOS and are included in Fig. 1. We see that the error from the fixed-node approximation is largest in the crossover region, at intermediate values of  $x$ . The maximum error is about 10% of the “correlation energy”, the difference between the BCS and exact energies.

In addition to serving as a benchmark for theory, the new EOS can provide validation for experiments. Exper-

iments are fast developing; in 3D remarkable precision [7] was reached in the measurement of the Bertsch parameter (with uncertainties only slightly larger than our symbol size in the top panel of Fig. 1). In the inset in the bottom panel, we show a comparison of the calculated pressure with the latest experiment in 2D [28]. In the crossover regime, better agreement with experiment is seen with the new result than with DMC. There may be other factors contributing to the discrepancy between experiment and theory [30, 31]. We leave more detailed comparisons of our results and experiment to a future publication.

We parametrize the computed EOS by  $E_c \equiv E_{\text{QMC}} - E_{\text{BCS}}$  [note that  $E_{\text{BCS}}/E_{\text{FG}}$  is related to the two-body binding energy by  $1 - \epsilon_B/(2E_{\text{FG}})$ , and is given by  $1 - 8e^{-2(\gamma+x)}$  where  $\gamma = 0.57721$  is Euler's constant]:

$$\frac{E_c}{E_{\text{FG}}} = \begin{cases} f^l(x), & x \leq 0.2664; \\ f(x), & 0.2664 < x < 4.3058; \\ f^r(x), & x \geq 4.3058. \end{cases}$$

The intermediate region is fitted with a 7th-order polynomial

$$f(x) = \sum_{i=0}^7 a_i x^i. \quad (3)$$

In the BCS region, the form is based on perturbative results [32, 33]

$$f^r(x) = -\frac{1}{x} + \sum_{i=2}^4 \frac{a_i^r}{x^i}, \quad (4)$$

while in the BEC regime a dimer form is used

$$f^l(x) = -1 + \frac{0.5}{X} \left[ 1 - \frac{\ln(X)}{X} + \frac{c_1}{X} + \frac{\sum_{i=0}^2 a_i^l (\ln X)^i}{X^2} \right], \quad (5)$$

where  $X \equiv c_0 - 2x$  with  $c_0 = 3.703$  from the dimer scattering length  $\sim 0.557a$  given by few-body calculations [11], and  $c_1 = \ln(\pi) + 2\gamma + 0.5$ . The parameters in Eqs. (4) and (5) are determined by continuity conditions (value and first two derivatives) from Eq. (3). The parameters and the locations of the transition between different regions are then varied in a small range to further minimize the variance of the overall fit with the QMC data. The final parameters are listed in Table I [34].

The contact [35, 36] is important to the physics of dilute gases, and can potentially be measured experimentally [37, 38]. With the functional form of the EOS, it is straightforward to determine the contact:

$$\frac{C}{k_F^4} = \frac{1}{4} \frac{d(E/E_{\text{FG}})}{dx}. \quad (6)$$

The result is shown in Fig. 2. An alternative approach to obtain the contact parameter is from the tail of the

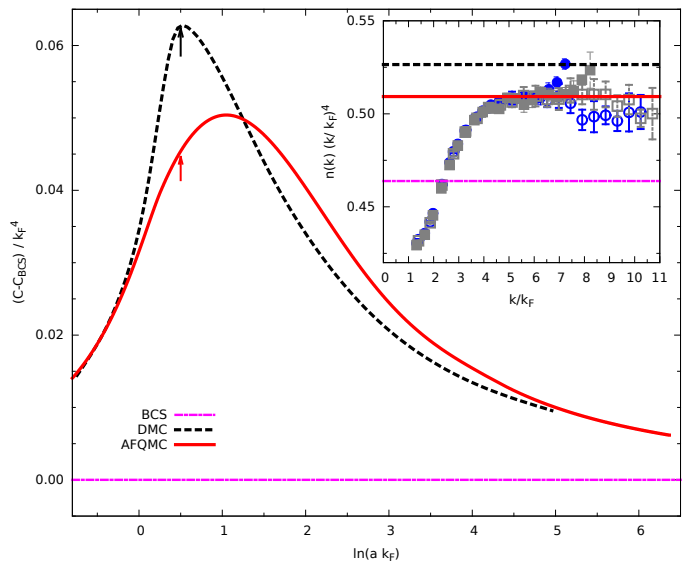


FIG. 2: (Color online) The contact parameter  $C$ . The main figure shows the result of  $C$  (relative to the BCS result) obtained from Eq. (6). The statistical uncertainty is smaller than the line thickness. DMC [18] and BCS results are also shown for comparison. The inset shows  $n(\mathbf{k})k^4$  vs  $k \equiv |\mathbf{k}|$  at  $x = 0.5$ . The horizontal lines give the  $C$  values from DMC, AFQMC and BCS (top to bottom), indicated by the arrows in the main figure. The  $n(\mathbf{k})$  data are from two systems, with  $L = 45$  (circles) and 51 (squares), respectively, and  $N = 58$ . Results are plotted for  $\mathbf{k}$  along both the horizontal (solid symbols) and diagonal (open) directions.

momentum distribution [36, 39]:  $n(\mathbf{k})k^4 \rightarrow C$  at large  $k$ . This provides an internal check on the consistency and accuracy of the calculation. As illustrated in the inset, a clear plateau is present before edge effects start to manifest as  $k$  approaches the cut-off value, giving a  $C$  value in excellent agreement with that from the EOS. (The full momentum distribution  $n(\mathbf{k})$  is shown in Fig. 3 for three representative interaction strengths.) The pressure and the chemical potential can be obtained from simple combinations of the energy and contact:  $P/P_{\text{FG}} = 2C/k_F^4 + E/E_{\text{FG}}$ , which was applied in the inset in Fig. 1, and  $\mu/\mu_{\text{FG}} = C/k_F^4 + E/E_{\text{FG}}$ .

We next quantify how the pairing properties evolve as a function of interaction strength. The zero-momentum pairing matrix (of dimension  $\mathcal{N}_s \times \mathcal{N}_s$ ),

$$M_{\mathbf{k}\mathbf{k}'} = \langle \Delta_{\mathbf{k}}^\dagger \Delta_{\mathbf{k}'} \rangle - \delta_{\mathbf{k}\mathbf{k}'} \langle c_{\mathbf{k}\uparrow}^\dagger c_{\mathbf{k}\uparrow} \rangle \langle c_{-\mathbf{k}\downarrow}^\dagger c_{-\mathbf{k}\downarrow} \rangle, \quad (7)$$

is computed in the many-body ground state, where the pair creation operator  $\Delta_{\mathbf{k}}^\dagger \equiv c_{\mathbf{k}\uparrow}^\dagger c_{-\mathbf{k}\downarrow}^\dagger$ . We associate [40] the leading eigenstate with the pair wave function in  $\mathbf{k}$ -space,  $\phi_{\uparrow\downarrow}(\mathbf{k})$ . This is shown in Fig. 3 for three characteristic interaction strengths. The inset shows the corresponding real-space structures,  $\psi_{\uparrow\downarrow}(\mathbf{r})$ , obtained from the Fourier transform of  $\phi_{\uparrow\downarrow}(\mathbf{k})$ . In the BEC regime, the momentum distribution is very broad, the pair wave function involves many  $\mathbf{k}$ -values, and the pairs are tightly

TABLE I: Final parameter values (full digits in Appendix D) in the parametrization [Eqs. (3-5)] of the exact EOS from QMC.

| $i$     | 0        | 1       | 2        | 3        | 4        | 5       | 6        | 7                       |
|---------|----------|---------|----------|----------|----------|---------|----------|-------------------------|
| $a_i^l$ | -11.8041 | 14.6755 | -4.85508 |          |          |         |          |                         |
| $a_i$   | -0.81984 | 0.12733 | 0.06851  | -0.01451 | -0.00919 | 0.00419 | -0.00064 | $3.4312 \times 10^{-5}$ |
| $a_i^r$ |          |         | -0.06085 | 0.36401  | -0.61531 |         |          |                         |

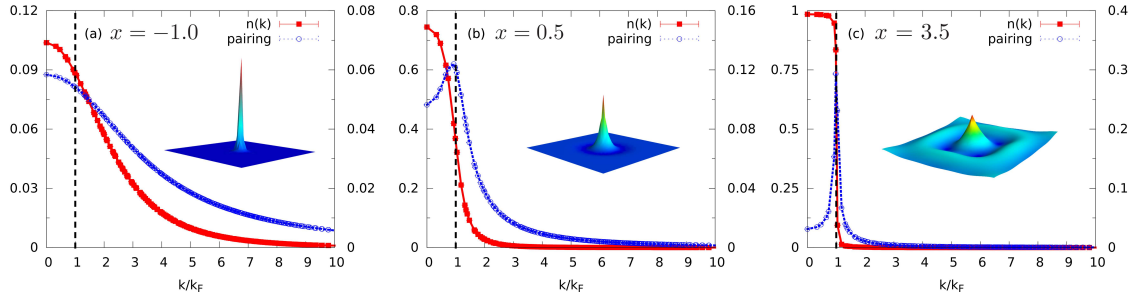


FIG. 3: (Color online) Momentum distribution and pair wave functions in three regimes of interaction strengths,  $x \equiv \ln(ak_F)$ . In each panel, the vertical tick labels on the left are for  $n(\mathbf{k})$  and those on the right are for  $\phi_{\uparrow\downarrow}(\mathbf{k})$ , both plotted vs.  $k$  (in units of  $k_F$ ). Note the different scales between the three panels. The inset shows the real-space wave function  $\psi_{\uparrow\downarrow}(\mathbf{r})$  vs.  $\mathbf{r}$  in a 3D plot. The lattice has  $N_s = 2025$  sites, with density  $n = 0.0286$ .

bound like a molecule, as seen in (a). In the BCS regime in (c), on the other hand, modifications to the non-interacting  $n(\mathbf{k})$  are limited to near the Fermi surface, with a small number of  $\mathbf{k}$ -vectors in its vicinity participating in pairing. The pair wave function is sharply peaked near the Fermi surface, and becomes very extended in real space. (Residual finite-size effect can be seen in this case in the second ring of  $\psi_{\uparrow\downarrow}(\mathbf{r})$  which is affected by the shape of the supercell.) As  $k_F a$  is increased, the systems crosses over from (a) to (c) via the strongly interacting regime represented in (b). Beyond the central peak, the wave function  $\psi_{\uparrow\downarrow}(\mathbf{r})$  in (b) contains significant radial oscillations, with multiple circular nodes.

The condensate fraction is given by the largest eigenvalue of  $M_{\mathbf{k}\mathbf{k}'}$  divided by  $N/2$ . The results are shown in Fig. 4 as a function of interaction. At the mean-field BCS level  $M_{\mathbf{k}\mathbf{k}'} = \langle \Delta_{\mathbf{k}}^\dagger \rangle \langle \Delta_{\mathbf{k}'} \rangle$ , and there is only one non-zero eigenvalue (equal to  $\sum_{\mathbf{k}} |\langle \Delta_{\mathbf{k}} \rangle|^2$ ). In the many-body ground state, additional depletion of the condensate is present from scattering into zero-momentum pairs distinct from  $\phi_{\uparrow\downarrow}(\mathbf{k})$ . The BCS condensate fraction and pair wave functions are in reasonable agreement with exact results down to  $\ln(ak_F) \sim 3$ . For stronger interactions, the BCS condensate fraction grows significantly faster. At  $\ln(ak_F) \sim -1$ , it predicts an essentially 100% condensate as opposed to only 80% from the exact result. In this regime, Bogoliubov theory of a Bose gas [41] with the dimer scattering length above gives results consistent with the QMC data. The largest deviation between BCS and exact results occurs in the crossover region, near  $\ln(ak_F) \sim 0.5$ , where the momentum distributions and pair wave functions also exhibit the largest differences.

We also calculate the real-space on-site pairing corre-

lation function:

$$C(\mathbf{r}) = \langle c_{\mathbf{0}\uparrow}^\dagger c_{\mathbf{0}\downarrow}^\dagger c_{\mathbf{r}\downarrow} c_{\mathbf{r}\uparrow} \rangle, \quad (8)$$

where the reference point  $\mathbf{0}$  and all  $\mathbf{r}$  values related by translational symmetry can be averaged over. The results are shown as a function of  $r \equiv |\mathbf{r}|$  in the inset in Fig. 4, for three representative values of interaction strength. Long-range order can be seen in all three regimes, with  $C(\mathbf{r})$  approaching a finite constant at large  $r$ .

In summary, we have calculated *exact* properties of the strongly interacting 2D Fermi gas at zero temperature, by a combination of two AFQMC methods. The equation of state, contact parameter, condensation fraction and pair wave functions are obtained. Improved agreement is seen with the pressure recently measured in quasi-2D experiment compared to best current (approximate) theoretical results. Our results will provide valuable benchmarks for future studies and allow precise comparisons with experiments as the latter rapidly develop in 2D. The analytic forms parametrized from the accurate numerical results will also facilitate future local-density type of calculations [42] in a variety of systems relevant to experiment, including thermodynamics and out of equilibrium properties in the presence of a trap. The technical advances in computational techniques, which allowed efficient sampling of larger lattices with long imaginary-times and much smaller Monte Carlo variance than previously possible, can be expected to have many applications in cold atom systems and elsewhere.



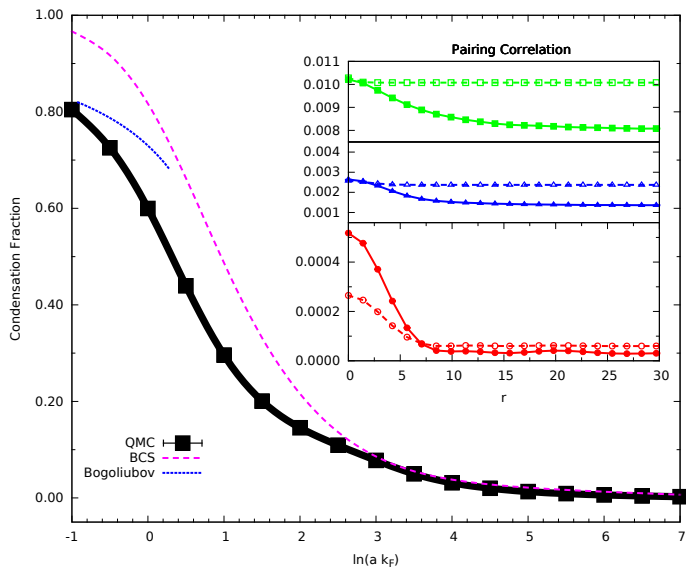


FIG. 4: (Color online) Condensate fraction and pairing correlation functions. In the main graph, the uncertainty in the QMC data (from extrapolation to the TL) is estimated by multiple runs with different sizes and is indicated by the thickness of the line. Also shown are BCS results and, in the BEC limit, Bogoliubov results for Bose gas for reference. In the inset, the pairing correlation function  $C(\mathbf{r})$  is plotted vs.  $r$  for three interaction strengths (from top to bottom, the same parameters as in (a), (b), and (c) of Fig. 3). The dashed lines are from BCS and solid lines are QMC results (error bars smaller than symbol size).

### Appendix A: Generalized Metropolis with force bias

In this appendix, we describe our second approach using the generalized Metropolis procedure to accelerate the sampling of paths in auxiliary field (AF) space. We introduce a dynamic force bias, analogous to what is employed in the branching random walk methods in constrained path or phase-free AFQMC [27], in proposing the updates of the field values, which improves the acceptance ratio and hence the MC efficiency.

To facilitate the description of the sampling algorithm we first give a brief sketch of the standard path-integral AFQMC approach, on which more detailed descriptions can be found in, for example, Refs. [43] and [27]. Ground state AFQMC measures the static properties by

$$\langle \hat{O} \rangle = \frac{\langle \psi_T | \exp(-\beta \hat{H}/2) \hat{O} \exp(-\beta \hat{H}/2) | \psi_T \rangle}{\langle \psi_T | \exp(-\beta \hat{H}) | \psi_T \rangle}, \quad (\text{A1})$$

where the Hamiltonian  $\hat{H} \equiv \hat{K} + \hat{V}$  is given by Eq. (1). We apply the usual Trotter-Suzuki breakup

$$e^{-\Delta\tau \hat{H}} \simeq e^{-\Delta\tau \hat{K}/2} e^{-\Delta\tau \hat{V}} e^{-\Delta\tau \hat{K}/2} \quad (\text{A2})$$

and the Hubbard-Stratonovich (HS) decomposition [44]

$$\begin{aligned} e^{\Delta\tau U n_{i\uparrow} n_{i\downarrow}} &= \frac{1}{2} \sum_{x_i = \pm 1} e^{(\gamma x_i - \Delta\tau U/2)(n_{i\uparrow} + n_{i\downarrow} - 1)} \quad (\text{A3}) \\ &\equiv \frac{1}{2} \sum_{x_i = \pm 1} \hat{b}_i(x_i), \end{aligned}$$

with  $\cosh(\gamma) = \exp(-\Delta\tau U/2)$ , arriving at the form

$$e^{-\Delta\tau \hat{H}} = \int d\mathbf{x} p(\mathbf{x}) \hat{B}(\mathbf{x}), \quad (\text{A4})$$

where  $\mathbf{x} = \{x_1, x_2, \dots, x_{N_s}\}$ . The probability density function  $p(\mathbf{x})$  is uniform for the  $2^{N_s}$  AF configurations under the choice of HS in Eq. (A3), and the one-body propagator is  $\hat{B}(\mathbf{x}) = e^{-\Delta\tau \hat{K}/2} \prod_i \hat{b}_i(x_i) e^{-\Delta\tau \hat{K}/2}$ .

The expression in Eq. (A1) is then re-written as a path integral of  $M \equiv \beta/\Delta\tau$  time slices. Let us consider the  $l$ -th time slice, and introduce the notation

$$\begin{aligned} \langle \psi_l | &= \langle \psi_T | \hat{B}(\mathbf{x}^{(M)}) \hat{B}(\mathbf{x}^{(M-1)}) \dots \hat{B}(\mathbf{x}^{(l+1)}) e^{-\Delta\tau \hat{K}/2} \\ | \psi_r \rangle &= e^{-\Delta\tau \hat{K}/2} \hat{B}(\mathbf{x}^{(l-1)}) \hat{B}(\mathbf{x}^{(l-2)}) \dots \hat{B}(\mathbf{x}^{(1)}) | \psi_T \rangle, \end{aligned}$$

which are both single Slater determinant wave functions if we choose  $|\psi_T\rangle$  to be a Slater determinant. The integrand of the path-integral in the denominator of Eq. (A1) then becomes

$$\mathcal{W}(\mathbf{x}) = p(\mathbf{x}) \langle \psi_l | \prod_{i=1}^{N_s} \hat{b}_i(x_i) | \psi_r \rangle, \quad (\text{A5})$$

where  $\mathbf{x}$  denotes the collection of AF at time slice  $l$ . In the standard way of sampling  $\mathcal{W}$ , one proposes to flip each auxiliary-field  $x_i$  one by one, and sweeps through  $\mathbf{x}$ . We will update the entire configuration  $\mathbf{x}$  (or a sub-cluster of  $\mathbf{x}$  for very large system sizes), simultaneously. We define a force bias [27]:

$$\bar{n}_{i\sigma} = \frac{\langle \psi_l | n_{i\sigma} | \psi_r \rangle}{\langle \psi_l | \psi_r \rangle}, \quad (\text{A6})$$

and propose updates of the fields with the probability density:

$$\mathcal{P}(\mathbf{x}) \propto p(\mathbf{x}) \prod_{i=1}^{N_s} e^{\gamma x_i (\bar{n}_{i\uparrow} + \bar{n}_{i\downarrow} - 1)} \quad (\text{A7})$$

which can be sampled directly. Detailed balance then leads to a Metropolis acceptance probability given by

$$\mathcal{A}(\mathbf{x} \rightarrow \mathbf{x}') = \min\left\{1, \frac{\mathcal{W}(\mathbf{x}') \mathcal{P}(\mathbf{x})}{\mathcal{W}(\mathbf{x}) \mathcal{P}(\mathbf{x}')}\right\}. \quad (\text{A8})$$

Note that the probability function for proposing transitions does not depend on the ‘‘current’’ configuration of AF, i.e.,  $\mathcal{P}(\mathbf{x} \rightarrow \mathbf{x}') = \mathcal{P}(\mathbf{x}')$ . If  $\mathcal{P} = \mathcal{W}$ , all updates will be accepted. Because of the force bias,  $\mathcal{P}$  approximates

$\mathcal{W}$  up to  $\mathcal{O}(\sqrt{\Delta\tau})$ , leading to typically high acceptance ratio.

Although we have used the discrete charge HS decomposition, the algorithm generalizes straightforwardly to continuous HS transformations. We comment that the use of the dynamic force bias in Eq. (A6) effectively introduces a background subtraction [27, 45] in the decomposition of Eq. (A3). That is, if one were to employ the standard updating algorithms *without the force bias*, one would find Eq. (A3) much less efficient than a continuous charge decomposition which subtracts a constant background. This discrepancy in efficiency grows more as the system density decreases, which is especially relevant since the systems studied here are at the low density limit. (See Ref. [45] for an analysis of the efficiency of HS transformations, and Ref. [46] for discussion on how the dynamic force bias automatically introduces an optimal constant background shift.)

Some other features of our algorithm are:

- Since we always work in the dilute limit, the memory is saved by only storing the wave function and calculating the Green function on the fly. We divide the path of  $M$  slices into  $\sqrt{M}$  blocks, and only track one block each time. The wave function at the beginning of each block is stored. The largest number of wave functions stored in our code is  $\sim 2\sqrt{M}$ .
- The wave function is transformed between real and momentum space by fast Fourier transformation, so that all the one-body operators during projection are diagonal, and Green functions in different space are easily obtained.
- When we only need the energy, we separate it into kinetic and potential energy. They are diagonal either in momentum or real space, where we do not need to calculate the whole Green function. To improve statistics, we measure the energy anywhere along the path and combine them, including the mixed estimator on both side.
- The standard determinantal QMC formalism as sketched above turns out to have a divergence of the Monte Carlo variance. We discuss the variance problem and its solution separately elsewhere [47]. The solution involves the introduction of a bridge link, which we have implemented in the calculations presented here. The force bias and basic sampling algorithm described above remain unchanged.

## Appendix B: Extrapolation to the continuum limit

We have described the extrapolation procedure of our lattice results to the continuum limit, and the subsequent analysis to reach the thermodynamic limit. Here we illustrate the finite size extrapolation in few-body systems.

The extrapolation to the continuum limit, for a fixed number of particles, must be consistent and independent

TABLE II: Data of the equation of state in Fig. 1. The interaction strength, given in the first column, are  $\ln(ak_F) = y + \ln(2)/2$ , with  $y$  from  $-0.75$  to  $6$  (in increments of  $0.25$  up to  $y = 2$ , then increments of  $0.5$  up to  $y = 5$ ).

| $\ln(ak_F)$ | $E_{QMC}/E_{FG}$ | Error bar | $E_{BCS}/E_{FG}$ |
|-------------|------------------|-----------|------------------|
| -0.403426   | -5.512634        | 0.000619  | -4.651252        |
| -0.153426   | -3.262997        | 0.000487  | -2.427641        |
| 0.096574    | -1.884889        | 0.000325  | -1.078969        |
| 0.346574    | -1.027841        | 0.000453  | -0.260958        |
| 0.596574    | -0.487667        | 0.000335  | 0.235190         |
| 0.846574    | -0.137058        | 0.000272  | 0.536119         |
| 1.096574    | 0.096228         | 0.000203  | 0.718642         |
| 1.346574    | 0.256943         | 0.000167  | 0.829348         |
| 1.596574    | 0.371799         | 0.000162  | 0.896491         |
| 1.846574    | 0.456471         | 0.000141  | 0.937204         |
| 2.096574    | 0.521804         | 0.000173  | 0.961859         |
| 2.346574    | 0.572904         | 0.000111  | 0.976740         |
| 2.846574    | 0.647340         | 0.000103  | 0.990927         |
| 3.346574    | 0.700067         | 0.000067  | 0.997096         |
| 3.846574    | 0.737144         | 0.000128  | 0.997307         |
| 4.346574    | 0.767283         | 0.000099  | 0.997765         |
| 4.846574    | 0.793547         | 0.000068  | 1.000206         |
| 5.346574    | 0.813073         | 0.000053  | 1.000436         |
| 6.346574    | 0.842689         | 0.000036  | 1.000654         |

of the type of kinetic energy dispersion. For a two-body problem on the lattice, exact results can be obtained for large system sizes by mapping to a one-body problem in the center of mass system. The results are shown in Fig. 5(a), which fit well a 4th-order polynomial function in  $1/L$ . We see from the inset that the coefficient on the linear term is zero within numerical precision.

We also show the finite size effect in the four-body problem from QMC, in Fig. 5(b), reaching large lattice sizes. The same general behavior is seen as in the two-body problem. We have also studied the finite-size behavior of the BCS solution, finding similar trends but with different slopes. In the many-body system, our QMC data are consistent with these observations as well. They are thus fitted with a 4th-order polynomial function with a vanishing  $1/L$  coefficient, as described in the main text.

## Appendix C: Equation of state data

We list the data for the equation of state in Fig. 1. The QMC energy data are calculated by our branching random walk approach with BCS trial wave functions.

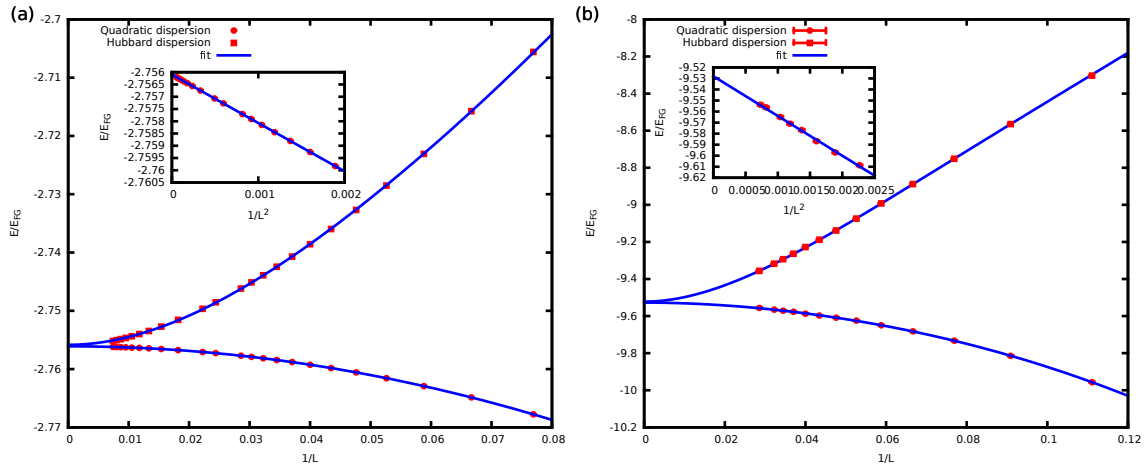


FIG. 5: (Color online) Extrapolation of finite-size lattice to the continuum limit in few body problems. Panel (a) shows exact diagonalization results for the two-body problem at  $\ln(ak_F) = 0.5$ , while panel (b) shows QMC solutions for the four-body problem at  $\ln(ak_F) = 0.0$ . In each case, results are obtained for both the Hubbard and the quadratic dispersions. A 4th-order polynomial function in  $1/L$  fits well both dispersions, and the extrapolated results in continuum limit agree well with each other. The insets indicate that the coefficients on  $1/L$  are negligible in both cases.

TABLE III: Final parameter values (full digits) in the parametrization [Eqs. (3-5)] of the exact EOS from QMC.

|         |                                    |
|---------|------------------------------------|
| $a_0^l$ | -11.804127317953723                |
| $a_1^l$ | 14.675499370762239                 |
| $a_2^l$ | -4.855080880566919                 |
| $a_0$   | -0.819842357425408                 |
| $a_1$   | 0.1273251139440354                 |
| $a_2$   | 0.0685123559420463                 |
| $a_3$   | -0.014505432043856327              |
| $a_4$   | -0.009191602440101383              |
| $a_5$   | 0.004190575139056055               |
| $a_6$   | -0.0006367374265820822             |
| $a_7$   | $3.431232818866204 \times 10^{-5}$ |
| $a_2^r$ | -0.060852400057644876              |
| $a_3^r$ | 0.36401186693517423                |
| $a_4^r$ | -0.61531422724189                  |

#### Appendix D: Full digits for Table I

#### Acknowledgments

We thank J. Carlson for useful discussions. This research was supported by DOE (grant no. de-sc0008627), NSF (grant no. DMR-1409510), and the Simons Foundation. Computing was carried out at the Oak Ridge Leadership Computing Facility at the Oak Ridge National Laboratory, which is supported by the Office of Science of the U.S. Department of Energy under Contract No. DE-AC05-00OR22725, and at the computational facilities at the College of William and Mary.

- [1] S. R. White, Phys. Rev. Lett. **69**, 2863 (1992).
- [2] U. Schollwöck, Rev. Mod. Phys. **77**, 259 (2005).
- [3] S. Giorgini, L. P. Pitaevskii, and S. Stringari, Rev. Mod. Phys. **80**, 1215 (2008), URL <http://link.aps.org/doi/10.1103/RevModPhys.80.1215>.
- [4] I. Bloch, J. Dalibard, and W. Zwerger, Rev. Mod. Phys. **80**, 885 (2008).
- [5] See, e.g., W. Ketterle and M. W. Zwierlein, *Making, probing and understanding ultracold Fermi gases*, in Ultracold Fermi Gases, Proceedings of the International School of Physics “Enrico Fermi”, Course CLXIV, Varenna, 20 - 30 June (2006), arXiv:0801.2500.
- [6] L. Luo and J. Thomas, Journal of Low Temperature Physics **154**, 1 (2009), ISSN 0022-2291.
- [7] M. J. H. Ku, A. T. Sommer, L. W. Cheuk, and M. W. Zwierlein, Science **335**, 563 (2012), <http://www.sciencemag.org/content/335/6068/563.full.pdf>, URL <http://www.sciencemag.org/content/335/6068/563.abstract>.
- [8] J. Carlson, S. Gandolfi, K. E. Schmidt, and S. Zhang, Phys. Rev. A **84**, 061602 (2011), URL <http://link.aps.org/doi/10.1103/PhysRevA.84.061602>.
- [9] Y. Nishida, Phys. Rev. A **79**, 013627 (2009), URL <http://link.aps.org/doi/10.1103/PhysRevA.79.013627>.
- [10] M. G. Endres, D. B. Kaplan, J.-W. Lee, and A. N. Nicholson, Phys. Rev. A **87**, 023615 (2013), URL <http://link.aps.org/doi/10.1103/PhysRevA.87.023615>.

- [11] D. S. Petrov, M. A. Baranov, and G. V. Shlyapnikov, Phys. Rev. A **67**, 031601 (2003), URL <http://link.aps.org/doi/10.1103/PhysRevA.67.031601>.
- [12] S. S. Botelho and C. A. R. Sá de Melo, Phys. Rev. Lett. **96**, 040404 (2006), URL <http://link.aps.org/doi/10.1103/PhysRevLett.96.040404>.
- [13] W. Zhang, G.-D. Lin, and L.-M. Duan, Phys. Rev. A **78**, 043617 (2008), URL <http://link.aps.org/doi/10.1103/PhysRevA.78.043617>.
- [14] J.-P. Martikainen and P. Törmä, Phys. Rev. Lett. **95**, 170407 (2005), URL <http://link.aps.org/doi/10.1103/PhysRevLett.95.170407>.
- [15] W. Zhang, G.-D. Lin, and L.-M. Duan, Phys. Rev. A **77**, 063613 (2008), URL <http://link.aps.org/doi/10.1103/PhysRevA.77.063613>.
- [16] J. Tempere, M. Wouters, and J. T. Devreese, Phys. Rev. B **75**, 184526 (2007), URL <http://link.aps.org/doi/10.1103/PhysRevB.75.184526>.
- [17] G. J. Conduit, P. H. Conlon, and B. D. Simons, Phys. Rev. A **77**, 053617 (2008), URL <http://link.aps.org/doi/10.1103/PhysRevA.77.053617>.
- [18] G. Bertaina and S. Giorgini, Phys. Rev. Lett. **106**, 110403 (2011), URL <http://link.aps.org/doi/10.1103/PhysRevLett.106.110403>.
- [19] A. A. Orel, P. Dyke, M. Delehaye, C. J. Vale, and H. Hu, New Journal of Physics **13**, 113032 (2011), URL <http://stacks.iop.org/1367-2630/13/i=11/a=113032>.
- [20] K. Martiyanov, V. Makhalov, and A. Turlapov, Phys. Rev. Lett. **105**, 030404 (2010), URL <http://link.aps.org/doi/10.1103/PhysRevLett.105.030404>.
- [21] M. Sato, Y. Takahashi, and S. Fujimoto, Phys. Rev. Lett. **103**, 020401 (2009), URL <http://link.aps.org/doi/10.1103/PhysRevLett.103.020401>.
- [22] J. B. Anderson, The Journal of Chemical Physics **65**, 4121 (1976).
- [23] D. M. Ceperley and B. J. Alder, The Journal of Chemical Physics **81**, 5833 (1984), URL <http://scitation.aip.org/content/aip/journal/jcp/81/12/10.1063/1.447637>.
- [24] F. Werner and Y. Castin, Phys. Rev. A **86**, 013626 (2012), URL <http://link.aps.org/doi/10.1103/PhysRevA.86.013626>.
- [25] S. Zhang, J. Carlson, and J. E. Gubernatis, Phys. Rev. Lett. **74**, 3652 (1995).
- [26] S. Zhang and H. Krakauer, Phys. Rev. Lett. **90**, 136401 (2003), URL <http://link.aps.org/doi/10.1103/PhysRevLett.90.136401>.
- [27] S. Zhang, *Auxiliary-Field Quantum Monte Carlo for Correlated Electron Systems*, Vol. 3 of *Emergent Phenomena in Correlated Matter: Modeling and Simulation*, Ed. E. Pavarini, E. Koch, and U. Schollwöck (Verlag des Forschungszentrum Jülich, 2013).
- [28] V. Makhalov, K. Martiyanov, and A. Turlapov, Phys. Rev. Lett. **112**, 045301 (2014), URL <http://link.aps.org/doi/10.1103/PhysRevLett.112.045301>.
- [29] We have applied finite-size corrections to our QMC results using the difference between the BCS energy for the same  $N$  and at the TL. The correction is in general small (largest at large  $x$ ) and vanishes with increasing  $N$ .
- [30] M. Bauer, M. M. Parish, and T. Enns, Phys. Rev. Lett. **112**, 135302 (2014), URL <http://link.aps.org/doi/10.1103/PhysRevLett.112.135302>.
- [31] J. Levinsen and M. M. Parish, ArXiv e-prints (2014), 1408.2737.
- [32] J. R. Engelbrecht, M. Randeria, and L. Zhang, Phys. Rev. B **45**, 10135 (1992), URL <http://link.aps.org/doi/10.1103/PhysRevB.45.10135>.
- [33] L. He, Phys. Rev. A **90**, 053633 (2014), URL <http://link.aps.org/doi/10.1103/PhysRevA.90.053633>.
- [34] Note that our  $a_2^+$  has different sign from the DMC result [18], but is consistent with analytic results of  $-0.05908$  [32, 33].
- [35] S. Tan, Annals of Physics **323**, 2952 (2008), ISSN 0003-4916, URL <http://www.sciencedirect.com/science/article/pii/S0003491608000349>.
- [36] S. Tan, Annals of Physics **323**, 2971 (2008), ISSN 0003-4916, URL <http://www.sciencedirect.com/science/article/pii/S0003491608000349>.
- [37] Y. Sagi, T. E. Drake, R. Paudel, and D. S. Jin, Phys. Rev. Lett. **109**, 220402 (2012), URL <http://link.aps.org/doi/10.1103/PhysRevLett.109.220402>.
- [38] R. J. Wild, P. Makotyn, J. M. Pino, E. A. Cornell, and D. S. Jin, Phys. Rev. Lett. **108**, 145305 (2012), URL <http://link.aps.org/doi/10.1103/PhysRevLett.108.145305>.
- [39] J. E. Drut, T. A. Lähde, and T. Ten, Phys. Rev. Lett. **106**, 205302 (2011), URL <http://link.aps.org/doi/10.1103/PhysRevLett.106.205302>.
- [40] C. N. Yang, Rev. Mod. Phys. **34**, 694 (1962), URL <http://link.aps.org/doi/10.1103/RevModPhys.34.694>.
- [41] M. Schick, Phys. Rev. A **3**, 1067 (1971), URL <http://link.aps.org/doi/10.1103/PhysRevA.3.1067>.
- [42] See, e.g., A. Bulgac, Superfluid Local Density Approximation: A Density Functional Theory Approach to the Nuclear Pairing Problem, chapter in "Fifty Years of Nuclear Physics" R. A. Broglia and V. Zelevinsky, p. 100 (Singapore, World Scientific, 2013), arXiv:1204.2207.
- [43] F. F. Assaad, *Quantum Monte Carlo Methods on Lattices: The Determinantal method.*, Lecture notes of the Winter School on Quantum Simulations of Complex Many-Body Systems: From Theory to Algorithms. Publication Series of the John von Neumann Institute for Computing (NIC). NIC series Vol. 10. ISBN 3-00-009057-6 Pages 99-155.
- [44] J. E. Hirsch, Phys. Rev. B **28**, 4059 (1983).
- [45] H. Shi and S. Zhang, Phys. Rev. B **88**, 125132 (2013), URL <http://link.aps.org/doi/10.1103/PhysRevB.88.125132>.
- [46] W. Purwanto and S. Zhang, Phys. Rev. E **70**, 056702 (2004), URL <http://link.aps.org/doi/10.1103/PhysRevE.70.056702>.
- [47] H. Shi and S. Zhang, to be published (2015).